Performance of Positive Corona in Tree-Shaped Multi-Needle-to-Plane Configurations

M. Abdel-Salam, H. Ziedan, and S. Kamal El-deen
Electrical Engineering Department, Assiut University, Egypt

Abstract—This paper is aimed at investigating the electric field, the positive-corona onset-voltage and current-voltage relationship of tree-shaped multi-needle-to-plane configurations. The configurations include 1, 5, 9, 13 and 17 needles arranged in one, two and three layers. The well-known charge simulation method was used to calculate the electric field in the gap spacing between positively-stressed needle-arrangements and opposite ground plane. Based on the evaluated field values, the onset-voltage was calculated according to the criterion of sustained avalanche process to trigger a streamer within the ionization-zone surrounding the coronating needle. Three needle-arrangements of single, five and nine needles were stressed positively to measure the corona onset-voltage and current-voltage characteristics at different gap spacings. The agreement between the calculated and measured onset-voltage values is satisfactory with a deviation not exceeding 3.96%. For the same applied voltage, the corona current decreases with the increase of the number of needles for the same gap spacing. The obtained results are discussed in the light of discharge physics.

Keywords—Charge simulation, positive corona, streamer theory, tree-shaped electrodes, corona onset voltage

I. INTRODUCTION

A grounded tree-shaped array of multi sharp conducting points is often used for protection of structures against lightning strokes [1, 2]. In cloudy weather conditions, the electric field is enhanced at the array tips resulting in air ionization and ion production in the space above the array. Such space charge may suppress the growth of upward streamer-triggered leaders by array shielding or displace the downward leaders away from the structure [1, 2].

Multiple-needle positive corona electrodes arranged in one or several rows of needles were aimed at improving particle charging conditions in electrostatic precipitators [3]. The obtained results confirmed that regions of relatively compact space charge generated by each needle are separated by narrow zones of little or no charge. The extension of these zones can be diminished by increasing the applied voltage and/or reducing the distance between adjacent needles [3].

The filtration characteristics of a miniature electrostatic precipitator (ESP) for aerosol particles using saw-like electrodes were reported [4]. The corona current was higher for dual saw-like electrodes in comparison with single saw-like electrode stressed at the same applied voltage. Experimental results indicated that aerosol penetration through the tested precipitator decreased with increasing corona current or with decreasing flow rate through the ESP. To ensure higher collection efficiency of the ESP, negative polarity is recommended. For indoor precipitators, positive polarity is recommended because of lower ozone production [4].

The interaction among evenly spaced discharge spots existing along a negative corona-wire in air was simulated with a multiple point electrode whose point-to-point spacing is adjustable [5]. The points were arranged in a circular and linear pattern. Although the current-voltage characteristic curve for the multiple point electrode-to-plane geometry is different from that a single point-to-plane, the spark-over voltage values are the same for both geometries [5].

The profiles of positive and negative corona current density on the ground plane of multi-needle-to-plane gaps were measured in atmospheric air [6]. The needles were equally spaced in a linear pattern. For the same applied voltage, gap spacing and needle-to-needle spacing, the peak values of the profiles are higher for negative corona when compared with positive corona [6].

A multipoint arrangement was used [7] as the charging electrode in an electrostatic precipitator for sampling and control of nanoparticles and sub-micron particles. The precipitator had the advantage of low pressure drop and high particle collection efficiency [7].

The characteristics of negative corona discharge in single-needle and multi-needle-to plane configurations were investigated [8]. The characteristics include the onset-voltage and the current-voltage relationship as well as their dependency on the number of needles, the needles' height and tip radius, the needle to needle spacing and the gap spacing. The needles were arranged in line, triangular, square, pentagonal, hexagonal and square-meshed configurations. The electric field was found minimum near the central needle and increases at the needles in the direction outwards due to the shielding effect imposed on the central needle by the other needles [8].

The pulsed positive corona in a multi-point-to-plane configuration as influenced by the geometry and electrical circuit was investigated [9]. Smaller distances between adjacent pins cause mutual interaction between simultaneously propagating streamers. The optimum spacing for such interaction to cease was found 10 mm for 100 μm tip radius of the points [9].

Corresponding author: Mazen Abdel-Salam
e-mail address: mazen2000as@yahoo.com

In the present work, the many sharp points forming a tree-shaped array are arranged in one central needle surrounded by needles grouped in layers around the central one. Such arrays are being used for protection of structures against lightning strokes [1, 2]. The points forming the array are conventional sewing needles with hyperboloid tip. Several steps are sought to investigate the role played by the array in onset-streamers initiation and corona-current increase with the increase of the applied voltage. The first step is to assess how the electric field is calculated in the vicinity of the array tips. The well-known charge simulation technique [10-13] is used for calculating the electric field in the space between the stressed array and the opposite ground plane. The second step is to model mathematically the condition for a self-sustained positive discharge forming a streamer in order to calculate the onset voltage of corona developed at the array tips. The third step is to build a set-up to measure the corona onset voltage and current-voltage characteristics for different array arrangements. The last step is focused on comparing the calculated onset voltage values with those measured experimentally and discussing the obtained results in the light of discharge physics. Development of upward-streamers from tree-shaped arrays in presence of downward leader during a lightning stroke is currently investigated and the results will be published soon in a following paper.

II. METHOD OF ANALYSIS

A. Charge Simulation Technique for Electric Field Calculation

A.1. Single-Needle Array

Fig. 1 shows a stressed single-point array with height of h and hyperboloid tip positioned underneath ground plane at gap spacing s.

With the application of a positive applied voltage V_{app}, the point is charged positively and its surface charge is simulated by a set of N point charges (Q (j), j = 1, 2, 3 … N) located along the point axis (y-axis) [10-13] and distributed along the needle height following a geometrical series expressed as:

$$h = r_t * r_1^{(N-1)} \tag{1}$$

where r_t is the tip radius of the needle and r_1 is the base of the geometric series to be determined from Eq. (1). The x- and y-coordinates of these charges are $y_c(j)$, j = 1, 2, 3 …N and $x_c(j)$, j = 1, 2, 3 …N are expressed as:

$$x_c(j) = 0\,,\ j = 1, 2, \dots N \tag{2-a}$$

$$y_c(j) = s + \left(r_t . r_1^{(j-1)}\right), j = 1, 2, \dots N \tag{2-b}$$

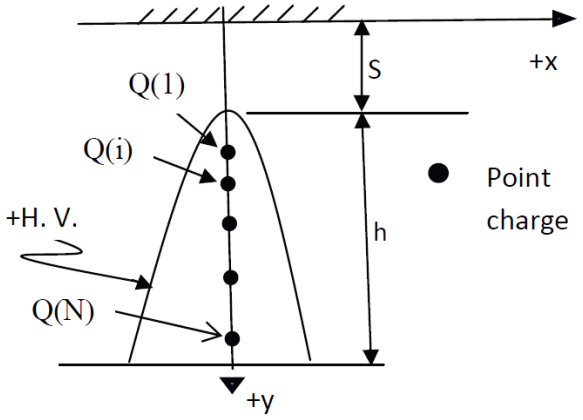

Fig. 1. Charge representation of a grounded needle against a stressed plane.

The geometrical series ensures high density of charges in the vicinity of the needle tip where the electric field is highly intensified.

To assess the values of the simulation charges, pertinent boundary conditions are satisfied at selected boundary points on the needle surface of coordinates $x_b(i)$, i = 1, 2, 3, … N and $y_b(i)$, i = 1, 2, 3, … N. The number of boundary points is equal to the number of simulation charges, where each boundary point corresponds to a simulation charge at the same y-level.

The coordinates of the i^{th} boundary point $x_b(i)$ and $y_b(i)$ satisfy the hyperboloid profile of the needle, which is expressed as [14]:

$$\frac{y_b{}^2(i)}{e_o{}^2.w_o{}^2} + \frac{x_b{}^2(i)}{e_o{}^2(1-w_o{}^2)} = 1 \tag{3-a}$$

$$e_o = \sqrt{s\left(1 + \frac{r_t}{s}\right)}\,, \quad w_o = \frac{1}{\sqrt{1+\frac{r_t}{s}}} \tag{3-b}$$

Because $y_b(i) = y_c(j)$, $i = j = 1, 2, \dots N$, the x-coordinate $x_b(i)$ is obtained using Eq. (3-a).

The boundary conditions are the Dirichlet condition, where the potential calculated at the needle surface is equal to the applied voltage and the potential of the grounded plane is equal to zero. To maintain the potential of the grounded plane at zero value, images of the simulation charges are considered.

The potential at the i^{th} boundary point is equal to the sum of the potentials produced at this point by the simulation charges and their images as expressed by the following equation:

$$\emptyset_i = \sum_{j=1}^{N} Q_j\,.P_{i,j} \tag{4}$$

where $P_{i,j}$ is the potential coefficient calculated at the i^{th} boundary point due to the j^{th} simulation charge and its image, which is expressed as [10, 13]:

$$P_{i,j} = \frac{1}{\sqrt{x_b{}^2(j)+(y_c(j)-y_b(i))^2}} - \frac{1}{\sqrt{x_b{}^2(j)+(y_c(j)+y_b(i))^2}} \tag{5}$$

The potential at all boundary points is equal to the applied voltage V_{app}. At the first boundary point (i = 1), the calculated potential due to all the simulation charges is equal to the applied voltage V_{app} as expressed as:

$$Q(1)P_{1,1} + Q(2)P_{1,2} + \cdots + Q(N)P_{1,N} = V_{app} \qquad (6)$$

Similar to the first boundary point, N equation(s) are written at the N-boundary points resulting in a set of equations whose solution determination the unknown simulation charges.

The x- and y-components of the electric field are expressed at point (x, y) as:

$$E_x = \sum_{j=1}^{N}\left[\frac{(x-x_c(j))}{(\sqrt{(x-x_c(j))^2+(y-y_c(j))^2})^3} - \frac{(x-x_c(j))}{(\sqrt{(x-x_c(j))^2+(y+y_c(j))^2})^3}\right]\frac{Q(j)}{4\pi\varepsilon_o} \qquad (7\text{-a})$$

$$E_y = \sum_{j=1}^{N}\left[\frac{(y-y_c(j))}{(\sqrt{(x-x_c(j))^2+(y_b-y_c(j))^2})^3} - \frac{(y+y_c(j))}{(\sqrt{(x-x_c(j))^2+(y+y_c(j))^2})^3}\right]\frac{Q(j)}{4\pi\varepsilon_o} \qquad (7\text{-b})$$

The total electric field is expressed as:

$$E_t = \sqrt{({E_x}^2 + {E_y}^2)} \qquad (7\text{-c})$$

To check the accuracy of the charge simulation procedure in satisfying the Dirichlet boundary condition, a set of N check points are located midway between the boundary points. The accuracy of the charge simulation procedure in satisfying the Dirichlet boundary condition at the needle surface is checked first. Then, the field distribution along the gap axis is determined. The field normality over the needle surface is another check of the solution accuracy. The integral of the electric field along the gap axis being equal to the applied voltage is a third check of the accuracy.

A.2. Multi-Needle Tree-Shaped Array

Different tree-shaped array configurations with many sharp points are arranged. Each array includes a central axial needle surrounded by inclined needles in one or more layer(s). The needles in each layer are uniformly distributed in the angular direction.

Fig. 2 shows side views of two- and three-layers needle arrangements. Figs. 3 and 4 show how the needle tips appear in Figs. 2-a and 2-b, respectively. In Fig. 4-a, the needles of the outer layer are aligned with those of

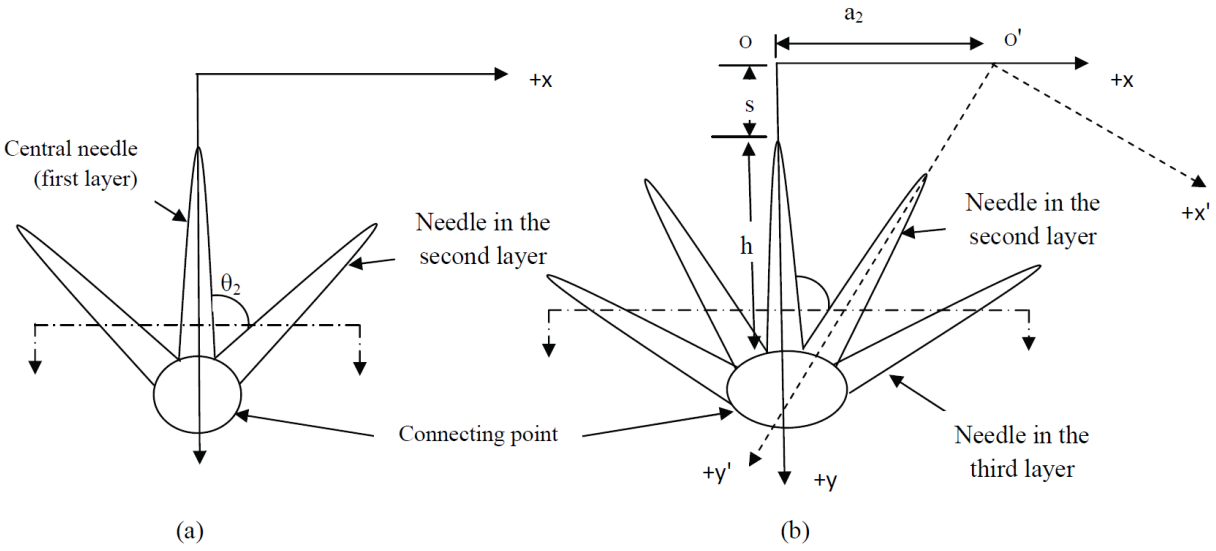

Fig. 2. Side view of multi-needle arrangements in (a) two layers and (b) three layers.

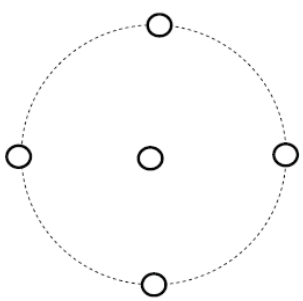

Fig. 3. Needles' tips appearance for 5 needles forming two-layer arrangement.

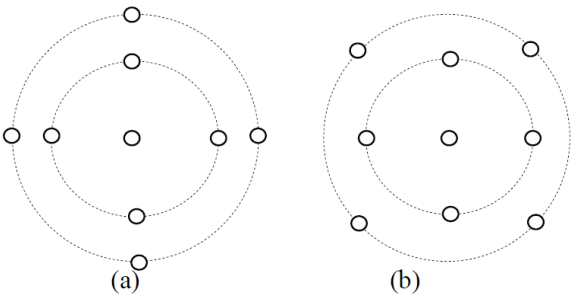

Fig. 4. Needles' tips appearance for 9 needles forming three-layer arrangement with (a) aligned needles and (b) crossed needles.

the inner layer. In Fig. 4-b, the needles of the outer layer are midway, so crossed with those of the inner layer.

To express the coordinates of the simulation charges of an inclined needle by an angle θ_2 among the second layer, the coordinate axes are moved distance (a_2) as shown in Fig. (2). The distance (a_2) is expressed as:

$$a_2 = (h+s)\tan(\theta_2) \tag{8}$$

Of course θ_1 and hence a_1 of the first layer are equal to zero.

The simulation charges and boundary points of the central needle are expressed in the *x*-, *y*- and *z*-coordinate system, Eq. (2). The coordinates of the simulation charges of the inclined needle in a new coordinate system (*x*', *y*', *z*') are related to those in the *x*-*y*-*z* coordinate system as reported in Appendix I.

The same as for the single-needle array, when stressed by the applied voltage, the array is charged and the surface charge per needle is simulated by point charges distributed along the axis of the needle. The number of simulation charges per needle changes from layer to layer; N_1, N_2 and N_3 for the first, second and third layers, respectively. For m_1, m_2 and m_3 needles in the first, second and third layers, total number of simulation charges are $m_1N_1+m_2N_2+m_3N_3$, where m_1 is always equal 1 corresponding to the central needle. The simulation charges along the needle axis are distributed following a geometrical series as described in the single-needle arrangement.

To assess the values of the simulation charges, boundary points are selected on the surface of one needle in each layer. This is because the needles of each layer are symmetrical in position and have the same surface charge distribution. The number of boundary points on each needle is equal to the number of the simulation charges of that needle. The boundary conditions are the Dirichlet one as in the single-needle arrangement. The check points were selected midway between the boundary points to check the accuracy of the charge simulation procedure in satisfying the Dirichlet boundary condition at each needle surface.

The electric field has three components (E_x-, E_y- and E_z-components) which are expressed at point (*x*', *y*', *z*') as [10, 13]:

$$E_x = \sum_{j=1}^{N}\left[\frac{(x\prime-x_{c}\prime(j))}{(\sqrt{(x\prime-x_{c}\prime(j))^2+(y\prime-y_{c}\prime(j))^2+(z\prime-z_{c}\prime(j))^2})^3} - \frac{(x\prime-xc\prime(j))}{(\sqrt{(x\prime-x_{c}\prime(j))^2+(y\prime-y_{c}\prime(j))^2+(z\prime+z_{c}\prime(j))^2})^3}\right]\frac{Q(j)}{4\pi\varepsilon_o} \tag{9-a}$$

$$E_y = \sum_{j=1}^{N}\left[\frac{(y\prime-y_{c}\prime(j))}{(\sqrt{(x\prime-x_{c}\prime(j))^2+(y\prime-y_{c}\prime(j))^2+(z\prime-z_{c}\prime(j))^2})^3} - \frac{(y\prime-y_{c}\prime(j))}{(\sqrt{(x\prime-x_{c}\prime(j))^2+(y\prime-y_{c}\prime(j))^2+(z\prime+z_{c}\prime(j))^2})^3}\right]\frac{Q(j)}{4\pi\varepsilon_o} \tag{9-b}$$

$$E_z = \sum_{j=1}^{N}\left[\frac{(z\prime-z_{c}\prime(j))}{(\sqrt{(x\prime-x_{c}\prime(j))^2+(y\prime-y_{c}\prime(j))^2+(z\prime-z_{c}\prime(j))^2})^3} - \frac{(z\prime+z_{c}\prime(j))}{(\sqrt{(x\prime-xc\prime(j))^2+(y\prime-y_{c}\prime(j))^2+(z\prime+z_{c}\prime(j))^2})^3}\right]\frac{Q(j)}{4\pi\varepsilon_o} \tag{9-c}$$

The total electric field is expressed as:

$$E_t = \sqrt{({E_x}^2 + {E_y}^2 + {E_z}^2)} \tag{9-d}$$

B. Onset Voltage Calculation

The models for calculating the positive corona onset voltage in non-uniform field gaps are based on the streamer theory [15–17]. According to this theory, corona occurs when an electron avalanche of a critical size results in a self-sustained positive discharge forming a streamer.

The streamer model first proposed by Loeb [16] for the uniform field was later modified for the non-uniform field [17]. The model is based on the assumption that, at corona onset voltage, the number of electrons N_1 in the primary avalanche is equal to the number of electrons N_2 in the secondary successor avalanches generated due to photonization process in the ionization zone around the tip of the stressed needle, i.e.;

$$N_2 \geq N_1 \tag{10}$$

The ionization zone boundary defines where the ionization coefficient α exceeds the attachment coefficient η, which is $y = y_i$ along the *y*-axis. Expressions of α and η as dependent on air pressure and electric field intensity are expressed in Appendix II.

As shown in Fig. 5, the size of the primary avalanche along the *y*-axis n_1 (y) corresponding to step j of total k steps of avalanche growth is expressed as [18, 19]:

$$n_1(y) = e^{\int_{y=y_i}^{y=s}(\alpha(y)-\eta(y))\mathrm{d}y} = n_1(j) \tag{11}$$

The number N_1 at the end of the primary-avalanche growth is:

$$N_1 = n_1(s) \tag{12}$$

To evaluate the growth of the secondary successor

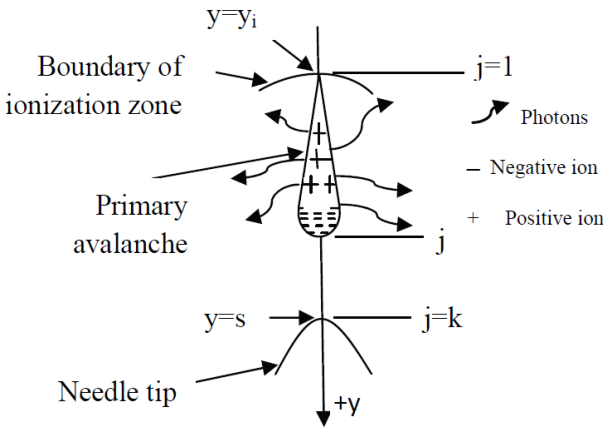

Fig. 5. Development of the primary avalanche.

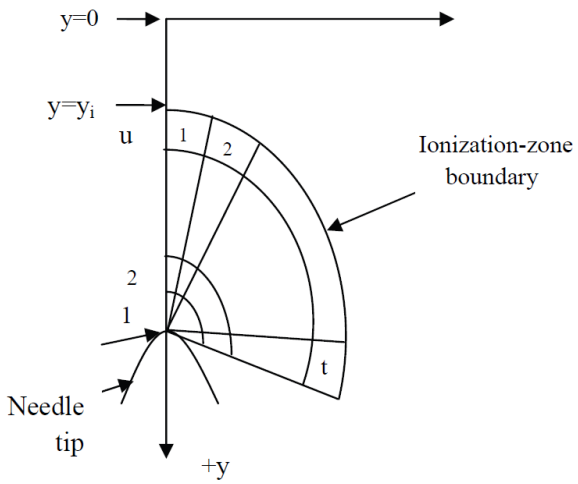

Fig. 6. Division of the ionization zone into *n* elements through *t* sectors and *u* divisions.

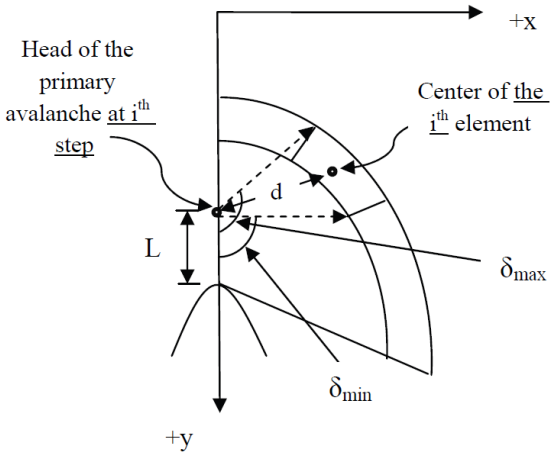

Fig. 7. Geometry factor details of an element.

avalanches, the ionization zone in the angular direction is sectionalized into *t* sectors as shown in Fig. 5. The radial lines defining the *t* sectors are divided into *u* divisions. Connection of the division points forms contours parallel to the ionization-zone boundary. The intersection of the radial lines with the contours results into *n* (= *u* * *t*) curvilinear rectangular elements, as shown in Fig. 6.

The number of electrons generated (by the action of the primary-avalanche-generated photons) in the i^{th} element of the ionization zone n_s (*i*) is expressed as [18, 19]

$$n_s(i) = \sum_{j=1}^{k} n_1(j) * \gamma_p * e^{-\mu * d} * g(i,j) \qquad (13)$$

where γ_p is Townsend's second coefficient, μ is the coefficient of photon absorption, *d* is the distance between the avalanche head at the j^{th} step and the center of the i^{th} element and *g*(*i*, *j*) is the geometry factor of the i^{th} element at the j^{th} step of the avalanche growth.

The geometry factor *g*(*i*, *j*) is calculated using the following equation:

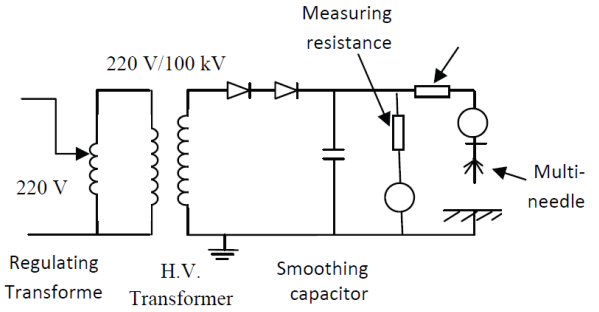

Fig. 8. Schematic diagram of the experimental set-up.

$$g(i,j) = \frac{1}{e^{-\mu * L}} * e^{-\mu * d * \beta} \qquad (14)$$

where *L* is the distance between the primary avalanche head and the needle tip and β (= δ_{max} - δ_{min}) is the difference between the maximum and minimum angles δ_{max} and δ_{min} defining the corners of the element, as shown in Fig. 7:

The number N_2 is expressed as:

$$N_2 = \sum_{i=1}^{n} e^{\int(\alpha(l)-\eta(l)).dl} . n_s(i) \qquad (15)$$

where *l* is the distance traveled by the secondary avalanche starting at the i^{th} element toward the central needle.

III. Experimental Set-up and Technique

A. Experimental Set-up

The experimental set-up shown in the schematic diagram of Fig. 8 consists of:

1. Regulating transformer with 220-V AC input voltage to feed a variable voltage to 100-kV high-voltage transformer through contactor switch.
2. H. V. transformer to step up the voltage to the desired value in the range 0-100 kV.
3. Half-wave rectifier circuit composed of two 20-mA, 140-kV PIV diodes to rectify the output of the H.V. transformer.
4. Smoothing capacitor to filter-out harmonics and generate DC voltage in the range 0-140 kV.
5. Water resistance to limit the current in case a spark breakdown happens.

B. Experimental Technique

To measure the corona onset voltage of single- and multi-needle configurations, a sensitive micro-ammeter was connected in series with the ground plane to determine the initiation of the corona discharge. The micro-ammeter reads down to 0.01 μA. The onset voltage corresponds to the applied voltage when the micro-ammeter starts to record a reading just above the zero value.

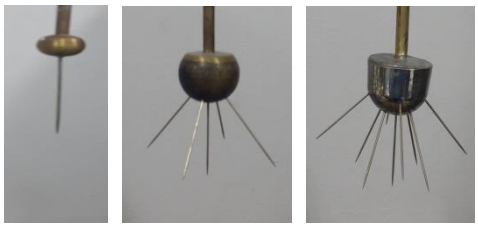

(a) (b) (c)

Fig. 9. Photographs of (a) single-, (b) five- and (c) nine-needle arrangements.

To measure the DC voltage applied to the multi-needle-to-plane configuration, a measuring resistance of 280 MΩ was connected to ground through a sensitive micro-ammeter, which reads down to 0.01 μA.

For all tested needle arrangements, the tip radius was constant at 0.045 mm and the gap spacing was varying in the range 0.03-0.13 m. Fig. 9 shows photographs of the single- , five- and nine-needle arrangements tested in the laboratory.

All measurements were recorded in an ambient air at temperature of 32±2°C and normal atmospheric pressure.

IV. Discussion

Seven needle arrangements for the investigated tree-shaped arrays are proposed. The needles are arranged in one central needle surrounded by needles grouped in layers around the central one. Each layer consists of needles distributed uniformly on a conical configuration, whose apex angle θ changes from layer to layer:

i) Single central needle as one-layer arrangement, $\theta_1 = 0^o$.
ii) Five needles (1 central + 4 surrounding needles in second layer) as a two-layer arrangement, $\theta_1 = 0^o$, $\theta_2 = 10^o$.
iii) Nine needles (1 central + 8 surrounding needles in second layer) as a two-layer arrangement, $\theta_1 = 0^o$, $\theta_2 = 10^o$.
iv) Nine needles (1 central + 4 surrounding needles in second layer + 4 surrounding needles in third layer) as a three-layer arrangement. The four needles of the outer layer are aligned with those of the inner layer, $\theta_1 = 0^o$, $\theta_2 = 10^o$ and $\theta_3 = 20^o$.
v) Nine needles (1 central + 4 surrounding needles in second layer + 4 surrounding needles in third layer) as a three-layer arrangement. The four needles of the outer layer are crossed to those of the inner layer, $\theta_1 = 0^o$, $\theta_2 = 10^o$ and $\theta_3 = 20^o$.
vi) Thirteen needles (1 central + 8 surrounding needles in second layer + 4 surrounding needles in third layer) as a three-layer arrangement, $\theta_1 = 0^o$, $\theta_2 = 10^o$ and $\theta_3 = 20^o$.
vii) Seventeen needles (1 central needle + 8 surrounding needles in second layer + 8 surrounding needles in third layer) as a three-layer arrangement, $\theta_1 = 0^o$, $\theta_2 = 10^o$ and $\theta_3 = 20^o$.

As a base case, the needle tip radius is 0.03 mm and the gap spacing is 3 mm. The tip radius and the gap spacing were changed in the ranges 0.01-0.03 mm and 0.3-15 cm, respectively. The number of the charges for all needles in a given layer is the same and changes from layer to layer. The number of charges is high for the central needle in the range 100-400 depending on the tip radius of the needles. The number of charges decreases form layer to layer in the range 70-250 for the second layer against 60-150 for the third layer. The number of charges per needle is independent of the gap spacing for the same tip radius.

A. Accuracy of Potential and Field Calculations

To check the accuracy of the charge simulation procedure in satisfying the Dirichlet boundary conditions, the percentage deviation of the calculated potential at the check points from the applied voltage value is calculated. The check points were chosen midway between the boundary points on the needles' surfaces. The potential deviation didn't exceed 0.008% for all investigated needle-arrangements.

The integral of the electric field along the gap axis starting from the tip of the central needle toward the ground plane is the second check to ensure the accuracy of the calculations; i.e.;

$$\int_{y=0}^{y=s} E(y)\mathrm{d}y = V_{app} \qquad (16)$$

where $E(y)$ is the field calculated along the y-axis of the gap and V_{app} is the applied voltage. The deviation of the integral of equation (15) from V_{app} didn't exceed 0.35 for the base case in all configurations.

The field normality is the third check to ensure the accuracy of the field calculations. The deviation of the field direction from being normal to the needle surface didn't exceed 6×10^{-6} for the base case in all configurations.

B. Electric Field as Influenced by Gap Geometry

B.1. Effect of Tip Radius

At a unit applied voltage (V_{app} = 1 kV), the field at the tip decreases with the increase of the tip radius for all investigated needle arrangements, as shown in the Figs. 10 and 11 for the same gap spacing. This is in conformity to the fact that the electric field is inversely proportional to the radius of curvature of the stressed electrode [20].

B.2. Effect of Number of Needles

At a unit applied voltage, Figs. 10 and 11 shows that the tip field of the central needle decreases with the increase of the number of the needles either in two- or

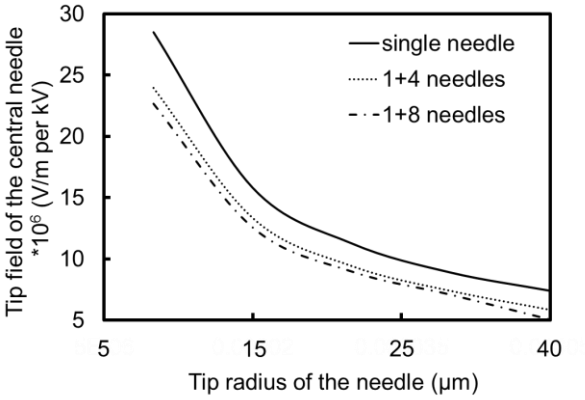

Fig. 10. Tip field of the central needle as influenced by the needle tip for first and second layers - gap spacing = 3 mm and V_{app} =1 kV.

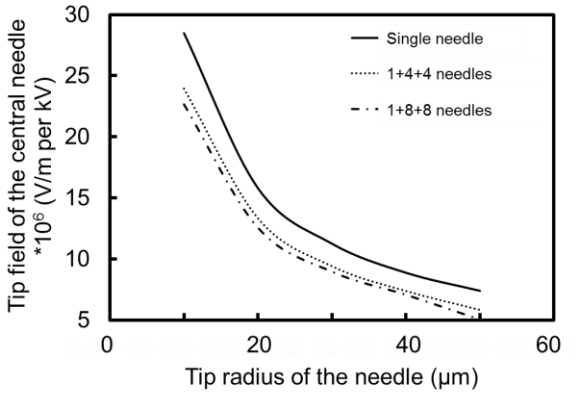

Fig. 11. Tip field of the central needle as influenced by the needle tip radius for first and third layers - gap spacing = 3 mm and V_{app} = 1 kV

TABLE I
TIP FIELD VALUES FOR THE INVESTIGATED NEEDLE ARRANGEMENTS AT UNIT APPLIED VOLTAGE

Arrangements	Field at the needle tip*10^7 (V/m per kV)		
	Layer 1	Layer 2	Layer 3
Single needle	1.1254	—	—
1+4 needles	0.939	0.9063	—
1+8 needles	0.895	0.821	—
1+4+4 aligned needles	0.918	0.85	0.743
1+4+4 crossed needles	0.925	0.8627	0.7668
1+8+4 aligned needles	0.890	0.796	0.720
1+8+8 aligned needles	0.848	0.782	0.67

three-layer arrangements, provided that the needle-tip radius and the gap spacing are constants. This is attributed to the shielding effect of the needles forming the second and third layers on the central needle. Such effect increases with the increase of number of needles and results in electric field reduction at the tip of the central needle, Figs. 10 and 11.

At a unit applied voltage, the field at the tip of the central needle remains higher than that of the other needles in the surrounding layers as given in Table I for the investigated needle arrangements. This is simply attributed to the smaller gap-spacing between the tip of the central needle and the ground plane when compared with that for the other surrounding needles. Subsequently the onset of corona always takes place at the tip of the central needle. This is in conformity to previous finding [5], where the occurrence of the sparking in multiple interacting point-to-plane gaps was observed between the central needle and the ground plane.

C. Corona Onset Voltage as Influenced by Gap Geometry

For all investigated needle arrangements, the onset of corona takes place always at the tip of the central needle. This is because not only the tip field but also the field within the ionization-zone around the tip are higher at the central needle when compared with that the other needles as indicated in Table I for the tip field values.

C.1. Effect of Tip Radius

The corona onset V_o voltage as a function of the tip radius at constant gap spacing is shown in Fig. 12 for different needle arrangements. The onset voltage increases with the increase of the needle tip radius. This is simply attributed to the corresponding decrease of the electric field within the ionization zone surrounding the central needle, Figs. 10 and 11. In this zone, the growth of the primary and secondary avalanches takes place as described above in section II. B.

C.2. Effect of Number of Needles

For the same tip radius and gap spacing, the corona onset voltage V_o increases with the increase of the number of needles surrounding the central one either in two or three layers. This is simply attributed to the above-mentioned shielding effect of the other needles on the central one with a subsequent reduction of the electric field, not only at the tip of the central needle Figs. 10 and 11, but also within the ionization-zone, where the primary and secondary avalanches grow. This is in agreement with previous findings, where the onset of corona from multiple-needle electrodes took place at a voltage higher than that of a single needle configuration [3]. This conforms to previous findings regarding corona in a multiple interacting point-to-plane gap in air [5], where the discharge at one point didn't effect that at the other points as long as the point-to-point spacing in much longer than the gap spacing. This is because there is no shielding effect among the points and every discharge point behaves separately. All of this confirms the obtained results as regards the impact of the surrounding needles on the electric field in the vicinity of the tip of the central needle and the resulting onset voltage of corona.

C.3. Effect of Gap Spacing

The corona onset voltage V_o as a function of the gap spacing at constant tip radius is shown in Fig. 13. The onset voltage increases with the increase of the gap spacing. This is attributed to the decrease of the applied electric field with the increase of gap spacing. Such

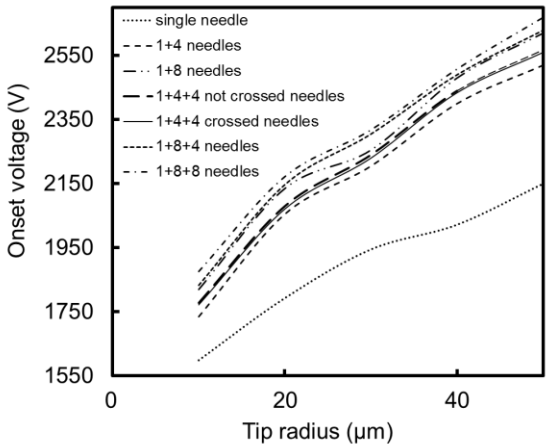

Fig. 12. Onset voltage as influenced by the tip radius at constant gap spacing.

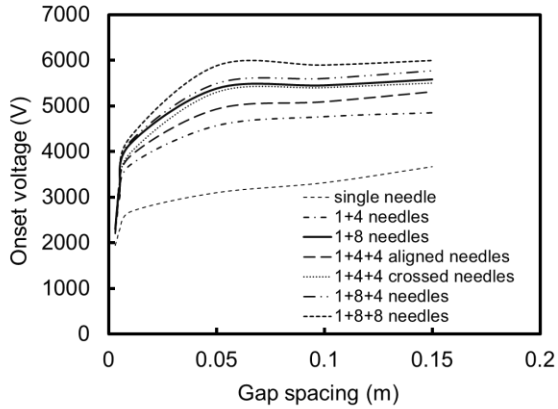

Fig. 13. Onset voltage as influenced by the gap spacing at constant tip radius.

decrease of the field results in shrinking the size of the ionization-zone around the central needle and increasing of the applied voltage which satisfies the onset criterion as expressed by Eq. (10).

D. Experimental Validation of Calculated Corona Onset Voltage Values

Table II gives the calculated corona onset-voltage V_o values in kV against those measured experimentally for single-, five- and nine-needle arrangements at varying gap spacing. The onset-voltage value increases with the increase of the gap spacing. This is simply attributed to the corresponding decrease of the electric field within the ionization-zone around the coronating needle. Within the ionization-zone, the primary avalanche and its successor avalanches grow and the condition expressed by Eq. (10) is satisfied at a lower voltage for longer gap spacing. The

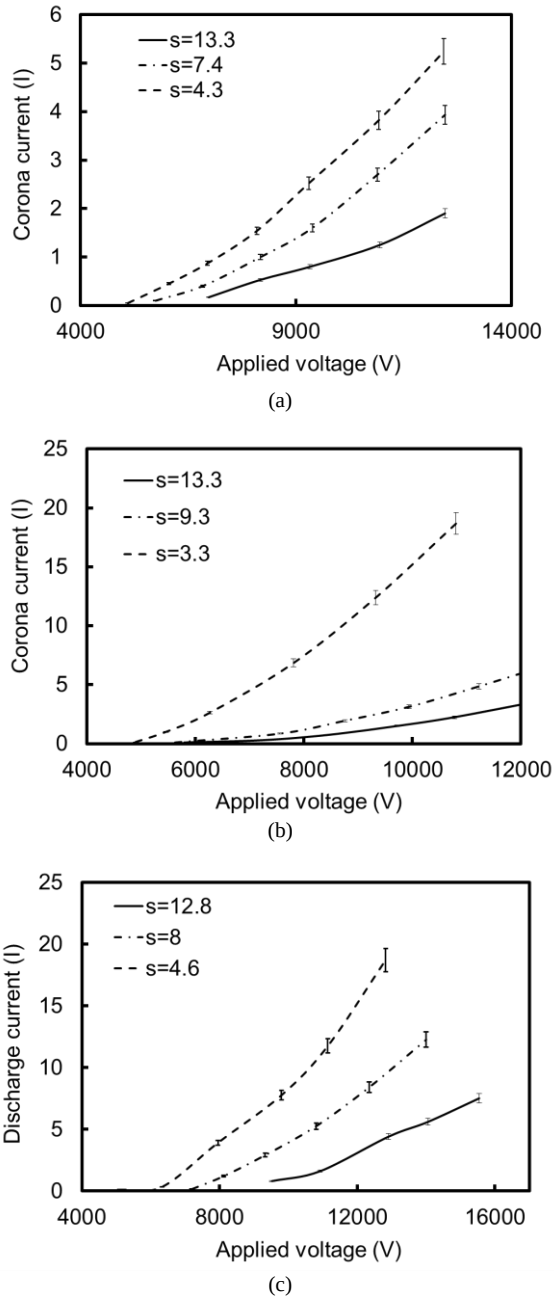

Fig. 14. Measured corona current-voltage characteristics for (a) single-, (b) five-, and (c) nine- needle arrangements at varying gap spacing.

onset-voltage increases with the increase of the number of needles at the same gap spacing. This is simply attributed to the shielding effect as mentioned before. The calculated onset-voltage values are always slightly higher than those measured experimentally for all tested needle arrangements. This is because the surface

TABLE II
CALCULATED ONSET-VOLTAGE VALUES AGAINST THOSE MEASURED EXPERIMENTALLY

	Single needle			1+4 needles			1+4+4 crossed needles		
s	13.3	7.3	4.3	13.3	9.3	3.3	12.8	8	4.6
V_{om}	4550	4500	4375	5550	5250	4750	7500	7000	4800
V_{oc}	4730	4550	4430	5700	5450	4833	7570	7250	4850
Dev.	-3.96	-1.11	-1.26	-2.7	-3.8	-1.75	-0.933	-3.57	-1.042

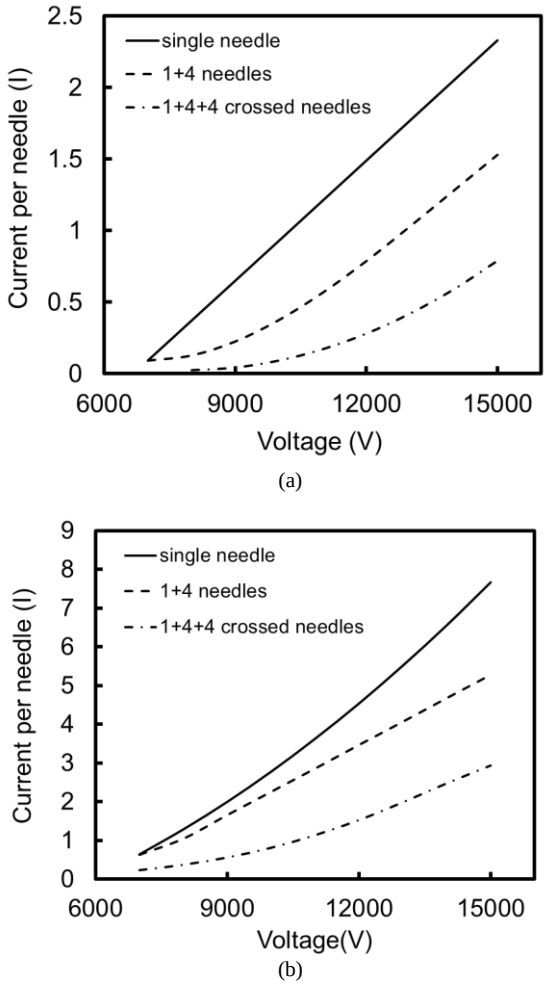

Fig. 15. Corona current per needle versus the applied voltage for single-, five- and nine- needle arrangements at gap spacing of (a) 0.04 m and (b) 0.12 m.

condition of the needles is assumed perfectly smooth in the calculations. The deviation between the calculated V_{oc} and measured V_{om} onset-voltage values did not exceed 3.96% as demonstrated at Table II.

E. Corona Current-Voltage Characteristics

Fig. 14 shows the measured corona current-voltage characteristics for (a) single-, (b) five-, and (c) nine-needle arrangements at varying gap spacing. The figure shows an increase of the corona onset-voltage with the increase of gap spacing for all tested arrangements in conformity to the calculated values in Fig. 13. For the same applied voltage value, the corona current in μA decreases with the increase of the gap spacing due to the subsequent decrease of the electric field within the gap spacing where corona ions convict from the needle arrangement to the ground plane. In previous publications [6, 7], the corona current from multi-needle electrode was found higher than that from single needle at the same applied voltage. The smaller the spacing between needles the lower is the corona current at the same applied voltage. This was attributed to the shielding effect imposed by the outer ones, such effect increases with the decrease of the spacing between the needles, the same as reported for discharge wires in wire-duct precipitators [21] and needles in multi-needle-to-plane configurations [8] stressed negatively. The total corona current increases with the increase of the number of needles at the same applied voltage in agreement with previous findings [9] even under positive pulsed applied voltages.

Fig. 15 shows the corona current per needle in μA versus the applied voltage for single-, five- and nine-needle arrangements at gap spacing of (a) 0.04 m and (b) 0.12 m, being interpolated from the measured values in Fig. 14. For the same applied voltage, the current per needle decreases with the increase of the number of needles irrespective of the value of the gap spacing. This confirms the above-mentioned shielding effect of the needles forming the second and third layers on the central needle. The corona current is assumed uniformly distributed among the needles of the arrangement in order to assess roughly the needle current for comparison purpose between the different needle arrangements.

V. CONCLUSION

1. A charge-simulation-based method is developed for calculating the electric field in tree-shaped multi-needle-to-plane configurations.
2. The calculation accuracy is satisfactory as regards to satisfaction of Drichlet condition and electric field normality at needles' surface.
3. The spatial distribution of the electric field along the gap axis is determined for different needle arrangements, tip radii and gap spacings. The calculation accuracy of the field values is satisfactory as regards to the equality of the integral of the calculated field along the gap spacing to the applied voltage value.
4. The electric field at the tip of the central needle decreases with the increase of the tip radius, gap spacing and number of needles.
5. For all investigated needle arrangements, the electric field at the tip of the central needle is higher than that at the other needles.
6. The onset of corona takes place at the tip of the central needle for all investigated needle arrangements.
7. The corona onset voltage increases with the increase of the needle tip radius at constant gap spacing and the increase of the gap spacing at constant tip radius.
8. The corona onset voltage increases with the increase of the number of needles because of the more shielding imposed from the outer needles on the central one. Subsequently, the onset voltage increases with the increase of number of layers around the central needle.
9. The calculated onset voltage values agreed satisfactorily with those measured experimentally

for single, five and nine needle arrangements at varying gap spacing in the range 0.045-0.135 m and constant tip radius of 0.045 mm.

ACKNOWLEDGMENT

The last author wishes to acknowledge Prof. Dr. M. TH. El-Mohandes for his kind help during my stay at the E. E. Department of Assuit University, Assiut.

REFERENCES

[1] W. Rison, "Experimental validation of conventional and nonconventional lightning protection systems," in *Power Engineering Society General Meeting, 2003, IEEE*, 2003, Vol. 4, pp. 1-6.

[2] A. Hossam-Eldin and M. Houssin, "Study of the effect of dissipation points on the lightning protection," *International Journal of Scientific and Technology Research*, vol. 1, pp. 46-51, 2012.

[3] L. Dascalescu, A. Samuila, D. Rafiroiu, A. Iuga, and R. Morar, "Multiple-needle corona electrodes for electrostatic processes application," *IEEE Transactions on Industry Applications*, vol. 35, pp. 543-548, 1999.

[4] S. H. Huang and C. C. Chen, "Filtration characteristics of a miniature electrostatic precipitator," *Aerosol Science and Technology*, vol. 35, pp. 792-804, 2001.

[5] L. C. Thanh, "Negative corona in a multiple interacting point-to-plane gap in air," *IEEE Transactions on Industry Applications*, vol. IA-21, pp. 518-522, 1985.

[6] M. T. El-Mohandes, S. Ushiroda, S. Kajita, Y. Kondo, and K. Horii, "Current density distribution on the plane electrode in a multineedle to plane configuration," in *Conference Record of the 1992 IEEE Industry Applications Society Annual Meeting*, 1992, pp. 1527-1532 vol.2.

[7] T.-C. Le, G. –Y. Lin, and C. –J. Tsai, "The predictive method for the submicron and nano-sized particle collection efficiency of multipoint-to-plane electrostatic precipitators," *Aerosol and Air Quality Research*, vol. 13, pp. 1404–1410, 2013.

[8] M. Abdel-Salam, A. Hashem, and E. Sidique, "Characteristics of negative corona discharge in single-needle- and multi-needle-to-plane configurations," *International Journal of Plasma Environmental Science and Technology*, vol. 7, pp. 121-135, 2013.

[9] M. M agureanu and N. B. Mandache, "Investigation of a pulsed positive corona in multi-point-to-plane configuration", in *Proc. of the 26th International conf. on Phenomena in Ionized Gases*, Greifswald, Germany, Vol. 7, 2003.

[10] H. Singer, H. Steinbigler, and P. Weiss, "A charge simulation method for the calculation of high voltage fields," *IEEE Transactions on Power Apparatus and Systems*, vol. PAS-93, pp. 1660-1668, 1974.

[11] N. H. Malik, "A review of the charge simulation method and its applications," *IEEE Transactions on Electrical Insulation*, vol. 24, pp. 3-20, 1989.

[12] M. Abdel-Salam, *et al*., *High-Voltage Engineering - Theory and Practice*, Marcel Dekker, Inc., 2nd Edition, Chapter 2, New York, USA, 2000.

[13] M. S. Abou-Seada and E. Nasser, "Digital computer calculation of the electric potential and field of a rod gap," *Proceedings of the IEEE*, vol. 56, pp. 813-820, 1968.

[14] W. L. Lama and C. F. Gallo, "Systematic study of the electrical characteristics of the "trichel" current pulses from negative needle-to-plane coronas," *Journal of Applied Physics*, vol. 45, pp. 103-113, 1974.

[15] M. Abdel-Salam, *et al*., *High-Voltage Engineering - Theory and Practice*, Marcel Dekker, Inc., 2nd Edition, Chapter 4, New York, USA, 2000.

[16] L. B. Loeb, *Electrical Coronas: Their Basic Physical Mechanisms*, University of California Press, Berkeley, CA, USA, 1965.

[17] E. Nasser, *Fundamental of Gaseous Ionization and Plasma Electronics*, J. Wiley, New York, USA, 1971.

[18] M. Abdel-Salam and N. L. Allen, "Onset voltage of positive glow corona in rod-plane gaps as influenced by temperature," *IEE Proceedings -Science, Measurement and Technology*, vol. 152, pp. 227-232, 2005.

[19] M. Abdel-Salam and P. Weiss, "Discharges in air from point electrodes in the presence of dielectric plates-theoretical analysis," *IEEE Transactions on Electrical Insulation*, vol. 27, pp. 320-333, 1992.

[20] W. H. Hayt and J. A. Buck, *Engineering Electromagnetics*, McGRAW-HILL international edition, 8th Ed, Chapter 2, 2010.

[21] M. Abdel-Salam and D. Wiitanen, "Calculation of corona onset voltage for duct-type precipitators," *IEEE Transactions on Industry Applications*, vol. 29, pp. 274-280, 1993.

[22] J. I. Merian and L. G. Kraige, *Engineering Mechanics Statics*, Vol. 1, 5th Edition, Von-Hoffman Press., New York, USA, pp. 464-466, 2002.

[23] M. P. Sarma and W. Janischewskyj, "D.C. corona on smooth conductors in air. Steady-state analysis of the ionisation layer," *Proceedings of the Institution of Electrical Engineers*, vol. 116, pp. 161-166, 1969.

APPENDIXES

Appendix I. Rotation of Coordinates Axes

The coordinates in the *z*-*x* plane of the j^{th} simulation charge of a needle of the second layer after rotation to the left are expressed as follows [22]:

$$x'(j) = x(j)\cos(\theta_2) - z(j)\sin(\theta_2) \quad j = 1,2,\dots N \tag{17-a}$$

$$y'(i) = 0 \tag{17-b}$$

$$z'(j) = x(j)\sin(\theta_2) - z(j)\cos(\theta_2) \tag{17-c}$$

The coordinates in the *z*-*x* plane of the j^{th} simulation charge of a needle of the second layer after rotation to right are expressed as follows:

$$x'(j) = x(j)\cos(\theta_2) + z(j)\sin(\theta_2) \quad j = 1,2,\dots N \tag{18-a}$$

$$y'(j) = 0 \tag{18-b}$$

$$z'(j) = -x(j)\sin(\theta_2) + z(j)\cos(\theta_2) \tag{18-c}$$

The coordinates in the *z*-*y* plane of the j^{th} simulation charge of a needle of the second layer after rotation to left are expressed as follows:

$$x'(j) = 0 \qquad j = 1,2,\dots N \tag{19-a}$$

$$y'(j) = y(j)\cos(\theta_2) - z(j)\sin(\theta_2) \tag{19-b}$$

$$z'(j) = y(j)\sin(\theta_2) + z(j)\cos(\theta_2) \tag{19-c}$$

The coordinates in the *z*-*y* plane of the j^{th} simulation charge of a needle of the second layer after rotation to right are expressed as follows:

$$x'(j) = 0 \qquad j = 1,2,\dots N \tag{20-a}$$

$$y'(j) = y(j)\cos(\theta_2) - z(j)\sin(\theta_2) \qquad (20\text{-b})$$

$$z'(j) = y(j)\sin(\theta_2) + z(j)\cos(\theta_2) \qquad (20\text{-c})$$

Appendix II. Discharge Parameters

In order to calculate the onset voltage of corona at atmospheric pressure, the equations relating α (cm^{-1}) and η (cm^{-1}) at pressure *p* (torr) to the electric field *E* (V/cm) were expressed as:

For the ionization coefficient α:

In the range where [23] $E/p < 60$ (V/cm.torr):

$$\frac{\alpha}{p} = 4.7786\,.\,e^{-221p/E} \qquad (21\text{-a})$$

In the range where [23] $60 \leq E/p \leq 240$ (V/cm.torr):

$$\frac{\alpha}{p} = 9.682\,.\,e^{-264.2\,p/E} \qquad (21\text{-b})$$

In the range where [17] $E/p > 240$ (V/cm.torr):

$$\frac{\alpha}{p} = 15\,.\,e^{-365\,p/E} \qquad (21\text{-c})$$

For the attachment coefficient (η) is calculated using the follows equation [23]:

$$\frac{\eta}{p} = 0.01298 - \left(0.54 * 10^{-3} \times \frac{E}{p}\right) + (0.8710^{-5} \times (E/p)^2) \qquad (21\text{-d})$$